Well-Balanced Positivity Preserving Central-Upwind Scheme for the Shallow Water System with Friction Terms

Alina Chertock*, Shumo Cui†, Alexander Kurganov‡ and Tong Wu§

Abstract

Shallow water models are widely used to describe and study free-surface water flow. Even though, in many practical applications the bottom friction does not have much influence on the solutions, the friction terms will play a significant role when the depth of the water is very small. In this paper, we study the Saint-Venant system of shallow water equations with friction terms and develop a well-balanced central-upwind scheme that is capable of exactly preserving its steady states. The scheme also preserves the positivity of the water depth. We test the designed scheme on a number of one- and two-dimensional examples that demonstrate robustness and high resolution of the proposed numerical approach. The data in the last numerical example correspond to the laboratory experiments reported in [L. Cea, M. Garrido, and J. Puertas, J. Hydrol, 382 (2010), pp. 88–102], designed to mimic the rain water drainage in urban areas containing houses. Since the rain water depth is typically several orders of magnitude smaller than the height of the houses, we develop a special technique, which helps to achieve a remarkable agreement between the numerical and experimental results.

Key words: Saint-Venant system, shallow water equations with friction terms, central-upwind scheme, well-balanced scheme.
AMS subject classification: 76M12, 65M08, 86-08, 35L65, 35L67.

1 Introduction

Shallow water equations are a set of hyperbolic partial differential equations derived by a vertical integration of Navier-Stokes equations. They are widely used in atmospheric sciences, oceanography, coastal engineering and many other fields. In shallow water flow models, the horizontal length scale is considered to be much larger than the vertical one. As the result, the vertical effect can be neglected leading to a considerable simplification in the momentum equation, in which the vertical pressure gradients are replaced by the hydrostatic pressure. The simplest, yet commonly

*Department of Mathematics, North Carolina State University, Raleigh, NC 27695, USA; chertock@math.ncsu.edu
†Mathematics Department, Tulane University, New Orleans, LA 70118, USA; scui2@tulane.edu
‡Mathematics Department, Tulane University, New Orleans, LA 70118, USA; kurganov@math.tulane.edu
§Mathematics Department, Tulane University, New Orleans, LA 70118, USA; twu2@tulane.edu

used, shallow water model is the Saint-Venant system [8], which in the two-dimensional (2-D) case reads:

$$\begin{cases} h_t + (hu)_x + (hv)_y = R, \\ (hu)_t + \left(hu^2 + \frac{1}{2}gh^2\right)_x + (huv)_y = -ghB_x, \\ (hv)_t + (huv)_x + \left(hv^2 + \frac{1}{2}gh^2\right)_y = -ghB_y, \end{cases} \tag{1.1}$$

where $h(x,y,t)$ is the water depth, $u(x,y,t)$ and $v(x,y,t)$ are the x- and y-components of the average velocity, $R(x,y,t)$ is the water source term, $B(x,y)$ is a function describing the bottom topography, g is the gravity constant.

Solving the shallow water system numerically is a challenging task due to several reasons. In the first place, many physically relevant solutions of (1.1) are small perturbations of steady states, characterized by a delicate balance between the flux and source terms. If the method does not accurately respect this balance, the numerical errors (which cannot be made too small on practically relevant grids) may cause a so-called numerical storm, in which the magnitude of artificial waves maybe larger than the magnitude of the solution itself. The second major difficulty is related to the computation of solutions when the water depth h is very small or even zero. In such a case, small numerical oscillations may lead to appearance of negative values of h, which in turn would typically cause a significant problem in evaluating the eigenvalues of the system (1.1), which are $u \pm \sqrt{gh}$ and $v \pm \sqrt{gh}$.

A good numerical method for the system (1.1) should thus be well-balanced (in the sense that it must exactly preserve physically relevant steady states) and positivity preserving (in the sense that the computed values of h must be positive). In the past two decades, many well-balanced scheme have been developed (see, e.g., [1,3–5,10,13,15,18,22,26–30,33]). Some of them preserve only the "lake at rest" steady state, that is, $u \equiv v \equiv 0$, $h+B \equiv$ constant, [1,3–5,10,13,15,18,22,27,28], other can preserve a non-flat steady state solution as well, [26, 29, 30, 33]. There are also well-balanced schemes that preserve the positivity of h, (see, e.g., [1, 3–5, 10, 15, 18, 27, 28]).

In this paper, we focus on studying the effects of the bottom friction terms in the shallow water model and thus we consider the following modified version of (1.1):

$$\begin{cases} (h)_t + (hu)_x + (hv)_y = R, \\ (hu)_t + \dfrac{\partial}{\partial x}\left(hu^2 + \dfrac{g}{2}h^2\right) + \dfrac{\partial}{\partial y}\left(huv\right) = -ghB_x - \dfrac{\tau_x}{\rho}, \\ (hv)_t + \dfrac{\partial}{\partial x}\left(huv\right) + \dfrac{\partial}{\partial y}\left(hv^2 + \dfrac{g}{2}h^2\right) = -ghB_y - \dfrac{\tau_y}{\rho}, \end{cases} \tag{1.2}$$

where τ_x and τ_y are the two components of the bottom friction and ρ is the water density. The friction terms are computed by using the following formulae:

$$\frac{\tau_x}{\rho} = ghI_x, \qquad \frac{\tau_y}{\rho} = ghI_y, \tag{1.3}$$

where the I_x and I_y are the components of the bottom friction slope given by the classical Manning formulation (see, e.g., [9]):

$$I_x = \frac{n^2}{h^{4/3}}\, u\sqrt{u^2+v^2}, \qquad I_y = \frac{n^2}{h^{4/3}}\, v\sqrt{u^2+v^2}, \tag{1.4}$$

where n is the Manning coefficient. Alternative friction terms were proposed in, e.g., [11, 14].

The system (1.2) still admits the "lake at rest" steady states. However, we are interested in simulating drainage of the rain water in urban areas. In such situations, the simplest yet physically relevant quasi one-dimensional (1-D) steady-state solutions correspond to the case when the water flows over a slanted infinitely long surface with a constant slope as illustrated in Figure 1.1 (left). Such steady states are discussed in §2.

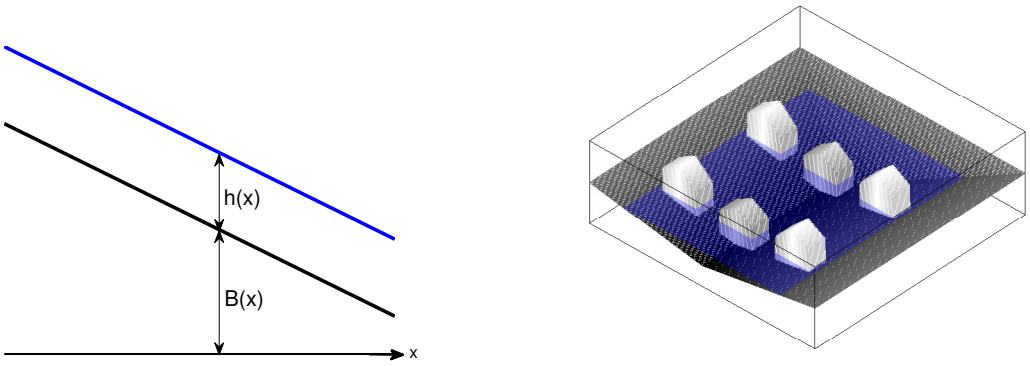

Figure 1.1: The bottom setting of numerical examples. The figure on the left corresponds to the quasi 1-D "lake at rest" steady state. The figure on the right illustrates the case of urban draining with obstacles like houses. The slope of the bottom and the height of the houses is out of scale.

In [7], a well-balanced Roe-type numerical scheme that exactly preserves such steady states was proposed. However, to maintain the positivity of the water depth h, the scheme in [7] requires one to use very small time steps and thus may not be robust in certain settings. Another Godunov-type scheme for the 1-D version of (1.2), that is, for the system (2.1) below, was proposed in [2]. Though this method does not suffer from restrictive time stepping, it is only capable of preserving "lake at rest" steady states.

In this paper, we develop a well-balanced and positivity preserving central-upwind scheme for the system (1.2), whose 1-D and 2-D steady-state solutions are described in §2. Central-upwind schemes have been proposed for general hyperbolic system of conversation law in [16, 17, 20, 21] and extended to the Saint-Venant system and related models in [15, 18, 19]. These schemes belong to the family of Godunov-type central schemes that are Riemann-problem-solver-free, robust and highly accurate. The extension of central-upwind schemes to the shallow water system (1.2) is very natural and it is derived in §3 and §4. The designed scheme is tested in a number of numerical experiments including the ones with realistic urban bottom topography structures, schematically shown in Figure 1.1 (right). The results presented in §5 demonstrate the superb performance of the proposed numerical method. The data in Example 4 correspond to the laboratory experiments reported in [6], designed to mimic the rain water drainage in urban areas containing houses. Since the rain water depth is typically several orders of magnitude smaller than the height of the houses, in Example 4a the proposed central-upwind scheme has been modified to accurately handle such situations as follows. First, the houses are removed from the computational domain, which becomes a punctured domain with many internal solid wall boundary pieces. Second, the rain water falling over the houses is redistributed to the areas near the edges of the houses. This helps to achieve a remarkable agreement between the numerical and experimental results.

2 Steady-States Solutions

In this section, we discuss steady-state solutions of the shallow water system (1.2). We begin with the simplest 1-D case, in which the system (1.2) reduces to

$$\begin{cases} (h)_t + (hu)_x = R, \\ (hu)_t + \left(hu^2 + \dfrac{1}{2}gh^2\right)_x = -ghB_x - g\dfrac{n^2}{h^{1/3}}|u|u. \end{cases} \tag{2.1}$$

In the situation when the water source is zero ($R \equiv 0$), the steady state solution satisfies the time-independent system:

$$\begin{cases} (hu)_x = 0, \\ \left(hu^2 + \dfrac{1}{2}gh^2\right)_x = -ghB_x - g\dfrac{n^2}{h^{1/3}}|u|u. \end{cases} \tag{2.2}$$

For smooth solutions of (2.2) one can obtain a nontrivial steady state in the form

$$hu \equiv \text{constant}, \quad h \equiv \text{constant}, \quad B_x \equiv \text{constant}.$$

This solution corresponds to the situation when the water flows over a slanted infinitely long surface with the constant slope. Indeed, if we assume that $B_x \equiv -C$, where $C > 0$ is a constant, and denote $hu \equiv q_0$, then the second equation of (2.2) can be rewritten as

$$\left(-\frac{q_0^2}{h^2} + gh\right) h_x = -ghC - g\frac{n^2}{h^{1/3}}|u|u, \tag{2.3}$$

and we obtain

$$h \equiv h_n = \left(\frac{n^2 {q_0}^2}{C}\right)^{3/10}, \quad hu \equiv q_0, \quad B_x \equiv -C, \tag{2.4}$$

where h_n is the so-called normal depth. A simple analysis of the ODE (2.4) shows that this steady state is expected to be stable in the super-critical case, that is, when h_n is below the critical depth h_c:

$$h_n < h_c := \left(\frac{q_0}{g}\right)^{1/3}. \tag{2.5}$$

The structure of 2-D steady states is substantially more complicated. However, the quasi 1-D steady state solutions:

$$h \equiv \text{constant}, \quad u \equiv \text{constant}, \quad v \equiv 0, \quad B_x \equiv \text{constant}, \quad B_y \equiv 0, \tag{2.6}$$

or

$$h \equiv \text{constant}, \quad u \equiv 0, \quad v \equiv \text{constant}, \quad B_x \equiv 0, \quad B_y \equiv \text{constant}. \tag{2.7}$$

are still physically relevant to the situation depicted in Figure 1.1.

In the next sections, we design both 1-D and 2-D central-upwind schemes that exactly preserve the above steady states (2.4), (2.6) and (2.7) respectively.

3 One-Dimensional Central-Upwind Scheme

In this section, we introduce a well-balanced and positivity preserving central-upwind scheme for the 1-D shallow water equations (2.1). The scheme is derived along the lines of [18]. We first rewrite the system (2.1) in an equivalent form in terms of water surface $w := h + B$ and the discharge hu:

$$\begin{cases} w_t + (hu)_x = R, \\ (hu)_t + \left[\dfrac{(hu^2)}{w-B} + \dfrac{g}{2}(w-B)^2\right]_x = -g(w-B)B_x - g\dfrac{n^2}{h^{1/3}}|u|u. \end{cases} \tag{3.1}$$

We use the notation

$$\mathbf{U} := \begin{pmatrix} w \\ hu \end{pmatrix}, \quad \mathbf{F}(\mathbf{U}, B) := \begin{pmatrix} hu \\ \frac{(hu^2)}{w-B} + \frac{g}{2}(w-B)^2 \end{pmatrix}, \quad \mathbf{S}(\mathbf{U}, R, B) := \begin{pmatrix} R \\ -g(w-B)B_x - g\frac{n^2}{h^{1/3}}|u|u \end{pmatrix},$$

so that the system (3.1) takes the following vector form:

$$\mathbf{U}_t + \mathbf{F}(\mathbf{U}, B)_x = \mathbf{S}(\mathbf{U}, R, B).$$

For simplicity, we introduce a uniform grid $x_\alpha := \alpha\Delta x$, where Δx is a small spatial scale and the corresponding finite volume cells $C_j := [x_{j-\frac{1}{2}}, x_{j+\frac{1}{2}}]$, and assume that at certain time level t, the solution is realized in terms of its cell averages,

$$\overline{\mathbf{U}}_j(t) = \frac{1}{\Delta x}\int\limits_{C_j} \mathbf{U}(x,t)\,dx.$$

A semi-discrete finite-volume scheme for computing $\overline{\mathbf{U}}_j$ is then written as the system of ODEs:

$$\frac{d}{dt}\overline{\mathbf{U}}_j(t) = -\frac{\mathbf{H}_{j+\frac{1}{2}}(t) - \mathbf{H}_{j-\frac{1}{2}}(t)}{\Delta x} + \overline{\mathbf{S}}_j(t), \tag{3.2}$$

where $\mathbf{H}_{j\pm\frac{1}{2}}$ are numerical fluxes approximating the flux function $\mathbf{F}(\mathbf{U}, B)$ at the cell interfaces, that is,

$$\mathbf{H}_{j\pm\frac{1}{2}}(t) \approx \mathbf{F}(\mathbf{U}, B)\Big|_{x_{j\pm\frac{1}{2}}} = \left((hu)\Big|_{x_{j\pm\frac{1}{2}}}, \left(\frac{(hu)^2}{w-B} + \frac{g}{2}(w-B)^2\right)\Big|_{x_{j\pm\frac{1}{2}}}\right)^T, \tag{3.3}$$

and $\overline{\mathbf{S}}_j$ is an appropriate discretization of the cell averages of the source term:

$$\overline{\mathbf{S}}_j(t) \approx \frac{1}{\Delta x}\int\limits_{C_j} \mathbf{S}(\mathbf{U}, R, B)\,dx.$$

The ODE system (3.2) is to be integrated numerically by a stable and sufficiently accurate ODE solver. In our numerical examples reported below, we have used the third-order strong preserving Runge-Kutta (SSP-RK) ODE solver, see [12].

In what follows, we describe the construction of the numerical fluxes $\mathbf{H}_{j\pm\frac{1}{2}}$ and source term $\overline{\mathbf{S}}_j$. We also suppress the time-dependence of all indexed quantities in order to shorten the notation.

Central-Upwind Numerical Fluxes. In this paper, we use the central-upwind fluxes from [17]. To this end, we first construct piecewise linear polynomials in each cell,

$$\widetilde{\mathbf{U}}_j(x)=\overline{\mathbf{U}}_j+(\mathbf{U}_x)_j(x-x_j),\quad \forall x\in C_j,\ \forall j,$$

and compute the right and left point values at $x=x_{j+\frac12}$ of this piecewise linear reconstruction,

$$\mathbf{U}^+_{j+\frac12}:=\overline{\mathbf{U}}_{j+1}-\frac{\Delta x}{2}(\mathbf{U}_x)_{j+1},\quad \mathbf{U}^-_{j+\frac12}:=\overline{\mathbf{U}}_j+\frac{\Delta x}{2}(\mathbf{U}_x)_j. \tag{3.4}$$

These values will be second-order accurate provided the numerical derivatives $(\mathbf{U}_x)_j$ are (at least) first-order accurate approximations of $\mathbf{U}_x(x,t)$. To ensure a non-oscillatory nature of the reconstruction, the numerical derivatives $(\mathbf{U}_x)_j$ are to be computed using a nonlinear limiter (see, e.g., [23–25, 31, 32]). In our numerical experiments reported in §5, we have used generalized minmod limiter:

$$(\mathbf{U}_x)_j=\text{minmod}\left(\theta\frac{\overline{\mathbf{U}}_j-\overline{\mathbf{U}}_{j-1}}{\Delta x},\ \frac{\overline{\mathbf{U}}_{j+1}-\overline{\mathbf{U}}_{j-1}}{2\Delta x},\ \theta\frac{\overline{\mathbf{U}}_{j+1}-\overline{\mathbf{U}}_j}{\Delta x}\right),\quad \theta\in[1,2], \tag{3.5}$$

where the minmod function is defined as:

$$\text{minmod}(z_1,z_2,\dots)=\begin{cases}\min\limits_j z_j, & \text{if } z_j>0\quad\forall j,\\ \max\limits_j z_j, & \text{if } z_j<0\quad\forall j,\\ 0, & \text{otherwise.}\end{cases}$$

and the parameter θ can be used to control the amount of numerical viscosity present in the resulting scheme. However, the use of a limiter does not guarantee the the positivity of $h^{\pm}_{j+\frac12}$.

To overcome this difficulty, we first replace the bottom topography function $B(x)$ with its continuous piecewise linear approximation $\widetilde{B}$:

$$\widetilde{B}(x)=B_{j-\frac12}+(B_{j+\frac12}-B_{j-\frac12})\cdot\frac{x-x_{j-\frac12}}{\Delta x},\quad x_{j-\frac12}\le x\le x_{j+\frac12}, \tag{3.6}$$

where

$$B_{j+\frac12}:=\frac{B(x_{j+\frac12}+0)+B(x_{j+\frac12}-0)}{2},$$

which reduces to $B_{j+\frac12}=B(x_{j+\frac12})$ if B is continuous at $x=x_{j+\frac12}$. Then the cell average over the cell C_j reads

$$B_j:=\widetilde{B}(x_j)=\frac{1}{\Delta}\int\limits_{C_j}\widetilde{B}(x)dx=\frac{B_{j+\frac12}+B_{j-\frac12}}{2}. \tag{3.7}$$

Remark 3.1 Notice that the piecewise linear reconstruction 3.6 will be exact for the slanted bottom topography which is a case of a special interest.

Next, we have to correct the reconstruction for w near (almost) dry areas since as it was shown in [18], the use of the original reconstruction (3.4) may produce negative values of $\widetilde{h}=\widetilde{w}-\widetilde{B}$. The correction procedure proposed in [18] does not allow one to preserve "lake at rest" steady states

in the presence of dry areas (like islands, shores, etc.). A more sophisticated correction procedure, which ensures that "lakes at rest" are always perfectly reconstructed has been recently proposed in [3].

In this paper we are, however, mostly concerned with a different type of steady-state solutions discussed in §2. Therefore, in the cells, where the original reconstruction (3.4) takes negative values of $\widetilde{h}$, we simply make the slope of h to be equal to the slope of B. Namely, we proceed as follows:

$$\begin{aligned}&\text{if } w^-_{j+\frac12} < B_{j+\frac12} \text{ or } w^+_{j-\frac12} < B_{j-\frac12}, \text{ then take } (w_x)_j = (B_x)_j\\ \Longrightarrow\quad & w^-_{j+\frac12} = \overline{h}_j + B_{j+\frac12}, \quad w^+_{j-\frac12} = \overline{h}_j + B_{j-\frac12},\end{aligned}$$

where $\overline{h}_j := \overline{w}_j - B_j$.

It should also be pointed out that near the dry-land area, the values of h could be very small or even zero which will not allow us to (accurately) compute the velocity $u^+_{j+\frac12} = \dfrac{(hu)^+_{j+\frac12}}{h^+_{j+\frac12}}$. To tackle this problem, we compute the velocity using the following desingularization formula:

$$u = \frac{2h(hu)}{h^2 + \max(h^2, \varepsilon)}, \tag{3.8}$$

where the superscripts $\pm$ and subscripts $j \pm \frac12$ are omitted and ε is a small a-priori chosen positive number, (roughly speaking, h is assumed to be almost dry if $h < \sqrt{\varepsilon}$). For consistency, the discharge is then recomputed:

$$(hu) := h \cdot u,$$

where u is obtained from (3.8).

Finally, equipped with the values of $h^\pm_{j+\frac12}$ and $u^\pm_{j+\frac12}$, the central-upwind fluxes are given by:

$$\mathbf{H}_{j+\frac12} = \frac{a^+_{j+\frac12}\mathbf{F}(\mathbf{U}^-_{j+\frac12}, B_{j+\frac12}) - a^-_{j+\frac12}\mathbf{F}(\mathbf{U}^+_{j+\frac12}, B_{j+\frac12})}{a^+_{j+\frac12} - a^-_{j+\frac12}} + \frac{a^+_{j+\frac12}a^-_{j+\frac12}}{a^+_{j+\frac12} - a^-_{j+\frac12}}\left[\mathbf{U}^+_{j+\frac12} - \mathbf{U}^-_{j+\frac12}\right], \tag{3.9}$$

where

$$\begin{aligned}a^+_{j+\frac12} &= \max\{u^+_{j+\frac12} + \sqrt{gh^+_{j+\frac12}}, u^-_{j+\frac12} + \sqrt{gh^-_{j+\frac12}}, 0\},\\ a^-_{j+\frac12} &= \min\{u^+_{j+\frac12} - \sqrt{gh^+_{j+\frac12}}, u^-_{j+\frac12} - \sqrt{gh^-_{j+\frac12}}, 0\},\end{aligned} \tag{3.10}$$

are the one-sided local speeds of propagation estimated from the largest and smallest eigenvalues of the Jacobian $\dfrac{\partial \mathbf{F}}{\partial \mathbf{U}}$.

Approximation of the Source Term. To discretize the source term, we calculate its first component using a midpoint rule so that

$$\overline{S}^{(1)}_j = R(x_j),$$

but approximate the geometric source using a special quadrature derived in [15, 18] (the friction term is also treated using the midpoint rule):

$$\overline{S}^{(2)}_j = -g\overline{h}_j\frac{B_{j+\frac12} - B_{j-\frac12}}{\Delta x} - 4gn^2\frac{|u_j|u_j}{\overline{h}_j^{1/3}}. \tag{3.11}$$

Here, again u_j is computed using the same desingularization process (3.8):

$$u_j = \frac{2\overline{h}_j(\overline{hu})_j}{\overline{h}_j^2 + \max(\overline{h}_j^2, \varepsilon)}, \tag{3.12}$$

Plugging (3.12) into (3.11) results in the following numerical source:

$$\overline{S}_j^{(2)} = -g\overline{h}_j\frac{B_{j+\frac{1}{2}} - B_{j-\frac{1}{2}}}{\Delta x} - 4gn^2\frac{|(\overline{hu})_j| \cdot (\overline{hu})_j \cdot \overline{h}_j^{5/3}}{\left[\overline{h}_j^2 + \max(\overline{h}_j^2, \varepsilon)\right]^2}, \tag{3.13}$$

which can now be applied in both wet and (almost) dry areas.

The proposed quadrature is indeed well-balanced in the sense that it exactly preserves the steady-state solution 2.4, where we assume

$$h = h_n, \quad hu = q_0, \quad B_x = -C \quad \text{and} \quad R \equiv 0. \tag{3.14}$$

In such a case, the numerical derivatives of $\mathbf{U}$ will be given by

$$(\mathbf{U}_x^{(1)}) = B_x, \qquad (\mathbf{U}_x^{(2)})_j = 0,$$

and the numerical flux will reduce to:

$$\mathbf{H}_{j+\frac{1}{2}} = \left(q_0, \frac{q_0^2}{h_n} + \frac{g}{2}h_n^2\right).$$

Therefore

$$\frac{\mathbf{H}_{j+\frac{1}{2}} - \mathbf{H}_{j-\frac{1}{2}}}{\Delta x} = 0,$$

which implies that the steady state solution (3.14) is exactly preserved by the numerical scheme as long as the second component of the source term equals 0, that is,

$$\overline{S}_j^{(2)} = gh_nC - 4gn^2\frac{q_0^2h_n^{5/3}}{[h_n^2 + \max(h_n^2, \varepsilon)]^2} = 0.$$

This can be proven true when $h_n > \varepsilon$ according to the definition of h_n in (2.4). Thus, the 1-D scheme we proposed preserves the steady state solution (3.14).

4 Two-Dimensional Central-Upwind Scheme

In this section, we describe the central-upwind scheme for the 2-D shallow water system (1.2). As in the 1-D case, we denote the water surface by $w := B + h$ and rewrite the system (1.2) in terms of the new unknown vector $\mathbf{U} = (w, hu, hv)^T$:

$$\mathbf{U}_t + \mathbf{F}(\mathbf{U}, B)_x + \mathbf{G}(\mathbf{U}, B)_y = \mathbf{S}(\mathbf{U}, R, B), \tag{4.1}$$

where the fluxes and the source terms are:

$$\begin{aligned}
\mathbf{F}(\mathbf{U},B)&=\left(hu,\frac{(hu)^2}{w-B}+\frac{1}{2}g(w-B)^2,\frac{(hu)(hv)}{w-B}\right)^T,\\
\mathbf{G}(\mathbf{U},B)&=\left(hv,\frac{(hu)(hv)}{w-B},\frac{(hv)^2}{w-B}+\frac{1}{2}g(w-B)^2\right)^T,\\
\mathbf{S}(\mathbf{U},R,B)&=\left(R,-(w-B)B_x-g\frac{n^2}{h^{1/3}}u\sqrt{u^2+v^2},-(w-B)B_y-g\frac{n^2}{h^{1/3}}v\sqrt{u^2+v^2}\right)^T.
\end{aligned}\tag{4.2}$$

We denote by $C_{j,k}$ the computational cells $C_{j,k}=[x_{j-\frac{1}{2}},x_{j+\frac{1}{2}}]\times[y_{k-\frac{1}{2}},y_{k+\frac{1}{2}}]$, where $x_\alpha=\alpha\Delta x$ and $y_\beta=\beta\Delta y$, and write a central-upwind semi-discretization of (4.1), (4.2) as the system of ODEs:

$$\frac{d}{dt}\overline{\mathbf{U}}_{j,k}=-\frac{\mathbf{H}^x_{j+\frac{1}{2},k}-\mathbf{H}^x_{j-\frac{1}{2},k}}{\Delta x}-\frac{\mathbf{H}^y_{j,k+\frac{1}{2}}-\mathbf{H}^y_{j,k-\frac{1}{2}}}{\Delta y}+\overline{\mathbf{S}}_{j,k},\tag{4.3}$$

for the time evolution of the cell averages:

$$\overline{\mathbf{U}}_{j,k}(t)=\frac{1}{\Delta x\Delta y}\iint\limits_{C_{j,k}}\mathbf{U}(x,y,t)\,dx\,dy.$$

The components in (4.3) are constructed as follows.

Central-Upwind Numerical Fluxes. As in the 1-D case, we follow [17] and obtain the numerical fluxes in the form:

$$\begin{aligned}
\mathbf{H}^x_{j+\frac{1}{2},k}=&\frac{a^+_{j+\frac{1}{2},k}\mathbf{F}(\mathbf{U}^E_{j,k},B_{j+\frac{1}{2},k})-a^-_{j+\frac{1}{2},k}\mathbf{F}(\mathbf{U}^W_{j+1,k},B_{j+\frac{1}{2},k}))}{a^+_{j+\frac{1}{2},k}-a^-_{j+\frac{1}{2},k}}+\frac{a^+_{j+\frac{1}{2},k}a^-_{j+\frac{1}{2},k}}{a^+_{j+\frac{1}{2},k}-a^-_{j+\frac{1}{2},k}}[\mathbf{U}^W_{j+1,k}-\mathbf{U}^E_{j,k}],\\
\mathbf{H}^y_{j,k+\frac{1}{2}}=&\frac{b^+_{j,k+\frac{1}{2}}\mathbf{G}(\mathbf{U}^N_{j,k},B_{j,k+\frac{1}{2}}))-b^-_{j,k+\frac{1}{2}}\mathbf{G}(\mathbf{U}^S_{j,k+1},B_{j,k+\frac{1}{2}}))}{b^+_{j,k+\frac{1}{2}}-b^-_{j,k+\frac{1}{2}}}+\frac{b^+_{j,k+\frac{1}{2}}b^-_{j,k+\frac{1}{2}}}{b^+_{j,k+\frac{1}{2}}-b^-_{j,k+\frac{1}{2}}}[\mathbf{U}^S_{j,k+1}-\mathbf{U}^N_{j,k}].
\end{aligned}\tag{4.4}$$

Here, $B_{j\pm\frac{1}{2},k}$ and $B_{j,k\pm\frac{1}{2}}$ are the values of the piecewise bilinear approximation $\widetilde{B}$ of the bottom topography function B at each cell $C_{j,k}$:

$$\begin{aligned}
\widetilde{B}(x,y)=&B_{j-\frac{1}{2},k-\frac{1}{2}}+(B_{j+\frac{1}{2},k-\frac{1}{2}}-B_{j-\frac{1}{2},k-\frac{1}{2}})\cdot\frac{x-x_{j-\frac{1}{2}}}{\Delta x}+(B_{j-\frac{1}{2},k+\frac{1}{2}}-B_{j-\frac{1}{2},k-\frac{1}{2}})\cdot\frac{y-y_{k-\frac{1}{2}}}{\Delta y}\\
&+(B_{j+\frac{1}{2},k+\frac{1}{2}}-B_{j+\frac{1}{2},k-\frac{1}{2}}-B_{j-\frac{1}{2},k+\frac{1}{2}}+B_{j-\frac{1}{2},k-\frac{1}{2}})\,\frac{(x-x_{j-\frac{1}{2}})(y-y_{k-\frac{1}{2}})}{\Delta x\Delta y},\quad (x,y)\in C_{j,k},
\end{aligned}\tag{4.5}$$

with

$$B_{j\pm\frac{1}{2},k\pm\frac{1}{2}}:=\frac{1}{2}\left(\max_{\xi^2+\eta^2=1}\lim_{h,l\to0}B(x_{j\pm\frac{1}{2}}+h\xi,y_{k\pm\frac{1}{2}}+l\eta)+\min_{\xi^2+\eta^2=1}\lim_{h,l\to0}B(x_{j\pm\frac{1}{2}}+h\xi,y_{k\pm\frac{1}{2}}+l\eta)\right).$$

As in the 1-D case (see (3.7)), the cell average of $\widetilde{B}$ over the cell $C_{j,k}$ is equal to its value at the center of the cell and is also equal to the average of the values of $\widetilde{B}$ at the midpoints of the edges

of $C_{j,k}$, namely we have:

$$B_{j,k} := \widetilde{B}(x_j, y_k) = \frac{1}{\Delta x \Delta y} \iint\limits_{C_{j,k}} \widetilde{B}(x,y)\,dx\,dy = \frac{1}{4}(B_{j+\frac{1}{2},k} + B_{j-\frac{1}{2},k} + B_{j,k+\frac{1}{2}} + B_{j,k-\frac{1}{2}}),$$

where

$$B_{j\pm\frac{1}{2},k} := \widetilde{B}(x_{j\pm\frac{1}{2}}, y_k) = \frac{1}{2}(B_{j\pm\frac{1}{2},k+\frac{1}{2}} + B_{j\pm\frac{1}{2},k-\frac{1}{2}}),$$

and

$$B_{j,k\pm\frac{1}{2}} := \widetilde{B}(x_j, y_{k\pm\frac{1}{2}}) = \frac{1}{2}(B_{j+\frac{1}{2},k\pm\frac{1}{2}} + B_{j-\frac{1}{2},k\pm\frac{1}{2}}).$$

Notice also that

$$B_{j\pm\frac{1}{2},k\pm\frac{1}{2}} = B\left(x_{j\pm\frac{1}{2}}, y_{k\pm\frac{1}{2}}\right),$$

if the function B is continuous at $(x_{j\pm\frac{1}{2}}, y_{k\pm\frac{1}{2}})$. For the slanted surface bottom we are presenting in Example 1 (illustrated in Figure 1.1), such approximation is exact.

The values $\mathbf{U}^{E,W,N,S}_{j,k}$ in (4.4) are the point values of the piecewise linear reconstruction $\widetilde{\mathbf{U}} = (\widetilde{w}, \widetilde{hu}, \widetilde{hv})$ for $\mathbf{U}$,

$$\widetilde{\mathbf{U}}(x,y) = \overline{\mathbf{U}}_{j,k} + (\mathbf{U}_x)_{j,k}(x - x_j) + (\mathbf{U}_y)_{j,k}(y - y_k), \quad (x,y) \in C_{j,k},$$

at $(x_{j+\frac{1}{2}}, y_k)$, $(x_{j-\frac{1}{2}}, y_k)$, $(x_j, y_{k+\frac{1}{2}})$, $(x_j, y_{k-\frac{1}{2}})$, respectively. Namely, we have:

$$\mathbf{U}^E_{j,k} := \widetilde{\mathbf{U}}(x_{j+\frac{1}{2}} - 0, y_k) = \overline{\mathbf{U}}_{j,k} + \frac{\Delta x}{2}(\mathbf{U}_x)_{j,k}, \quad \mathbf{U}^W_{j,k} := \widetilde{\mathbf{U}}(x_{j-\frac{1}{2}} + 0, y_k) = \overline{\mathbf{U}}_{j,k} - \frac{\Delta x}{2}(\mathbf{U}_x)_{j,k},$$
$$\mathbf{U}^N_{j,k} := \widetilde{\mathbf{U}}(x_j, y_{k+\frac{1}{2}} - 0) = \overline{\mathbf{U}}_{j,k} + \frac{\Delta y}{2}(\mathbf{U}_y)_{j,k}, \quad \mathbf{U}^S_{j,k} := \widetilde{\mathbf{U}}(x_j, y_{k-\frac{1}{2}} + 0) = \overline{\mathbf{U}}_{j,k} - \frac{\Delta y}{2}(\mathbf{U}_y)_{j,k}.$$

As in the 1-D case, the numerical derivatives $(\mathbf{U}_x)_{j,k}$ and $(\mathbf{U}_y)_{j,k}$ are first-order approximations of $\mathbf{U}_x(x_j, y_k, t)$ and $\mathbf{U}_y(x_j, y_k, t)$, respectively, and computed using a nonlinear limiter. In our numerical experiments, we have used the one-parameter family of the generalized minmod limiters with $\theta \in [1, 2]$:

$$\begin{aligned}(\mathbf{U}_x)_{j,k} &= \text{minmod}\left(\theta\frac{\overline{\mathbf{U}}_{j,k} - \overline{\mathbf{U}}_{j-1,k}}{\Delta x}, \frac{\overline{\mathbf{U}}_{j+1,k} - \overline{\mathbf{U}}_{j-1,k}}{2\Delta x}, \theta\frac{\overline{\mathbf{U}}_{j+1,k} - \overline{\mathbf{U}}_{j,k}}{\Delta x}\right),\\ (\mathbf{U}_y)_{j,k} &= \text{minmod}\left(\theta\frac{\overline{\mathbf{U}}_{j,k} - \overline{\mathbf{U}}_{j,k-1}}{\Delta y}, \frac{\overline{\mathbf{U}}_{j,k+1} - \overline{\mathbf{U}}_{j,k-1}}{2\Delta y}, \theta\frac{\overline{\mathbf{U}}_{j,k+1} - \overline{\mathbf{U}}_{j,k}}{\Delta y}\right).\end{aligned} \tag{4.6}$$

To preserve the positivity of water height h, we follow the 1-D approach presented in §3 and correct the reconstructed values of w as follows:

$$\text{if } w^E_{j,k} < B_{j+\frac{1}{2},k} \text{ or } w^W_{j,k} < B_{j-\frac{1}{2},k}, \text{ then take } (w_x)_{j,k} = (B_x)_{j,k} \tag{4.7}$$
$$\Longrightarrow w^E_{j,k} = B_{j+\frac{1}{2},k} + \overline{h}_{j,k}, \quad w^W_{j,k} = B_{j-\frac{1}{2},k} + \overline{h}_{j,k}; \tag{4.8}$$

$$\text{if } w^N_{j,k} < B_{j,k+\frac{1}{2}} \text{ or } w^S_{j,k} < B_{j,k-\frac{1}{2}}, \text{ then take } (w_y)_{j,k} = (B_y)_{j,k} \tag{4.9}$$
$$\Longrightarrow w^N_{j,k} = B_{j,k+\frac{1}{2}} + \overline{h}_{j,k}, \quad w^S_{j,k} = B_{j,k-\frac{1}{2}} + \overline{h}_{j,k}, \tag{4.10}$$

where $\overline{h}_{j,k} := \overline{w}_{j,k} - B_{j,k}$.

Once again, we observe that the obtained point values of h may be very small or even zero. The corresponding velocities should be thus calculated using a similar desingularization procedure:

$$u = \frac{2h(hu)}{h^2 + \max(h^2, \varepsilon)}, \quad v = \frac{2h(hv)}{h^2 + \max(h^2, \varepsilon)}, \tag{4.11}$$

where the superscripts E, W, N, S and subscripts (j,k) are omitted.

The local one-sided speeds of propagation $a^{\pm}_{j+\frac{1}{2},k}$ and $b^{\pm}_{j,k+\frac{1}{2}}$ in (4.4) can be computed using the eigenvalues of the Jacobians $\frac{\partial \mathbf{F}}{\partial \mathbf{U}}$ and $\frac{\partial \mathbf{G}}{\partial \mathbf{U}}$ as follows:

$$\begin{aligned}
a^{+}_{j+\frac{1}{2},k} &= \max\{u^{E}_{j,k} + \sqrt{gh^{E}_{j,k}},\ u^{W}_{j+1,k} + \sqrt{gh^{W}_{j+1,k}},\ 0\},\\
a^{-}_{j+\frac{1}{2},k} &= \min\{u^{E}_{j,k} - \sqrt{gh^{E}_{j,k}},\ u^{W}_{j+1,k} - \sqrt{gh^{W}_{j+1,k}},\ 0\},\\
b^{+}_{j,k+\frac{1}{2}} &= \max\{v^{N}_{j,k} + \sqrt{gh^{N}_{j,k}},\ v^{S}_{j,k+1} + \sqrt{gh^{S}_{j,k+1}},\ 0\},\\
b^{-}_{j,k+\frac{1}{2}} &= \min\{v^{N}_{j,k} - \sqrt{gh^{N}_{j,k}},\ v^{S}_{j,k+1} - \sqrt{gh^{S}_{j,k+1}},\ 0\}.
\end{aligned}$$

Approximation of the Source Term. The discretization of the source term is given by:

$$\begin{aligned}
\overline{\mathbf{S}}^{(1)}_{j,k} &= R(x_j, y_k),\\
\overline{\mathbf{S}}^{(2)}_{j,k} &= -g(\overline{w}_{j,k} - B_{j,k})\frac{B_{j+\frac{1}{2},k} - B_{j-\frac{1}{2},k}}{\Delta x} - gn^2\frac{u_{j,k}\sqrt{u^2_{j,k} + v^2_{j,k}}}{\overline{h}^{1/3}_{j,k}},\\
\overline{\mathbf{S}}^{(3)}_{j,k} &= -g(\overline{w}_{j,k} - B_{j,k})\frac{B_{j,k+\frac{1}{2}} - B_{j,k-\frac{1}{2}}}{\Delta y} - gn^2\frac{v_{j,k}\sqrt{u^2_{j,k} + v^2_{j,k}}}{\overline{h}^{1/3}_{j,k}},
\end{aligned} \tag{4.12}$$

where $u_{j,k}$ and $v_{j,k}$ are computed using the same desingularization process (4.11):

$$u_{j,k} = \frac{2\overline{h}_{j,k}(\overline{hu})_{j,k}}{\overline{h}^2_{j,k} + \max(\overline{h}^2_{j,k}, \varepsilon)}, \quad v_{j,k} = \frac{2\overline{h}_{j,k}(\overline{hv})_{j,k}}{\overline{h}^2_{j,k} + \max(\overline{h}^2_{j,k}, \varepsilon)}. \tag{4.13}$$

Substituting (4.13) into (4.12), the second and third terms of the numerical source term can be rewritten as follows:

$$\begin{aligned}
\overline{\mathbf{S}}^{(2)}_{j,k} &= -g(\overline{w}_{j,k} - B_{j,k})\frac{B_{j+\frac{1}{2},k} - B_{j-\frac{1}{2},k}}{\Delta x} - 4gn^2\frac{\sqrt{(\overline{hu})^2_{j,k} + (\overline{hv})^2_{j,k}}\cdot(\overline{hu})_{j,k}\cdot\overline{h}^{5/3}_{j,k}}{\left[\overline{h}^2_{j,k} + \max\{(\overline{h}^2_{j,k}, \varepsilon\}\right]^2},\\
\overline{\mathbf{S}}^{(3)}_{j,k} &= -g(\overline{w}_{j,k} - B_{j,k})\frac{B_{j,k+\frac{1}{2}} - B_{j,k-\frac{1}{2}}}{\Delta y} - 4gn^2\frac{\sqrt{(\overline{hu})^2_{j,k} + (\overline{hv})^2_{j,k}}\cdot(\overline{hv})_{j,k}\cdot\overline{h}^{5/3}_{j,k}}{\left[\overline{h}^2_{j,k} + \max\{(\overline{h}^2_{j,k}, \varepsilon\}\right]^2}.
\end{aligned}$$

As in 1-D case, one can prove that this quadrature exactly preserves the 2-D steady-state solution (3.14).

5 Numerical Examples

In this section, we test the designed well-balanced positivity preserving central-upwind scheme on several 1-D and 2-D problems including the ones with the data originating from the recently performed laboratory experiments reported in [6]. In all of the examples below, the gravitation constant $g = 9.8$ and the minmod parameter θ in (3.5) and (4.6) was set to be $\theta = 1.3$.

The solution was evolved in time using the third-order SSP-RK ODE solver (see [12]). In principle, the time step is to be chosen based on the CFL condition, that is,

$$\Delta t = \frac{\Delta x}{2a}, \quad a = \max_j \left\{ a^+_{j+\frac{1}{2}}, -a^-_{j+\frac{1}{2}} \right\}$$

in the 1-D case, and

$$\Delta t = \min\left\{ \frac{\Delta x}{2a}, \frac{\Delta y}{2b} \right\}, \quad a = \max_{j,k} \left\{ a^+_{j+\frac{1}{2},k}, -a^-_{j+\frac{1}{2},k} \right\}, \quad b = \max_{j,k} \left\{ b^+_{j,k+\frac{1}{2}}, -b^-_{j,k+\frac{1}{2}} \right\}$$

in the 2-D case. Since the flow may be very shallow (in which case $a \sim 0$ or $b \sim 0$), one needs to make sure that the time step is not taken to be too large. We therefore select

$$\Delta t = \min\left\{ \frac{1}{2a}, \frac{1}{10} \right\} \Delta x$$

in the 1-D case and

$$\Delta t = \min\left\{ \frac{\Delta x}{2a}, \frac{\Delta y}{2b}, \frac{\Delta x}{10}, \frac{\Delta y}{10} \right\}$$

in the 2-D case.

5.1 One-Dimensional Examples

Example 1 – Steady Flow Over a Slanted Surface. We begin by demonstrating the well-balance property of the designed scheme, that is, we test the ability of the scheme to exactly preserve the steady-state solution (3.14), which is schematically shown in Figure 1.1 (left). To this end, we consider the system (2.1) on interval $[0, 2.5]$ with $R \equiv 0$, $B_x \equiv -0.1$ and subject to the constant initial data given by (3.14). We introduce a uniform grid with $\Delta x = 0.025$ and set zero-order extrapolation boundary conditions at both ends of the domain. We run four sets of experiments with different values of h_n, q_0 and n taken from [6] and shown in Table 5.1. The solution is evolved until time $t = 100$. The right column of Table 5.1 clearly illustrates that our scheme preserves the studied steady-state solutions within machine accuracy.

Example 2 – Small Perturbation of Steady Flow Over a Slanted Surface. In this example, we introduce a small perturbation to the initial water surface in the steady states considered in Example 1:

$$h(x,0) = h_n + \begin{cases} 0.2h_n, & 1 \le x \le 1.25, \\ 0, & \text{otherwise}, \end{cases} \qquad (hu)(x,0) \equiv q_0. \tag{5.1}$$

We begin with a supercritical case (Test 2 in Table 5.1) and show the evolution of the computed solution in Figure 5.1. As one can see, at first the shape of the perturbation changes and it

Test	h_n	q_0	n	B_x	$\|h-h_n\|_\infty$
1	0.57708	2	0.02	-0.01	3.3307×10^{-16}
2	0.95635	0.1	0.02	-0.01	5.8287×10^{-16}
3	0.25119	0.1	0.1	-0.01	1.0547×10^{-15}
4	0.02402	0.002	0.1	-0.01	1.8978×10^{-15}

Table 5.1: The error in computing the steady-state solution (3.14) for different sets of data.

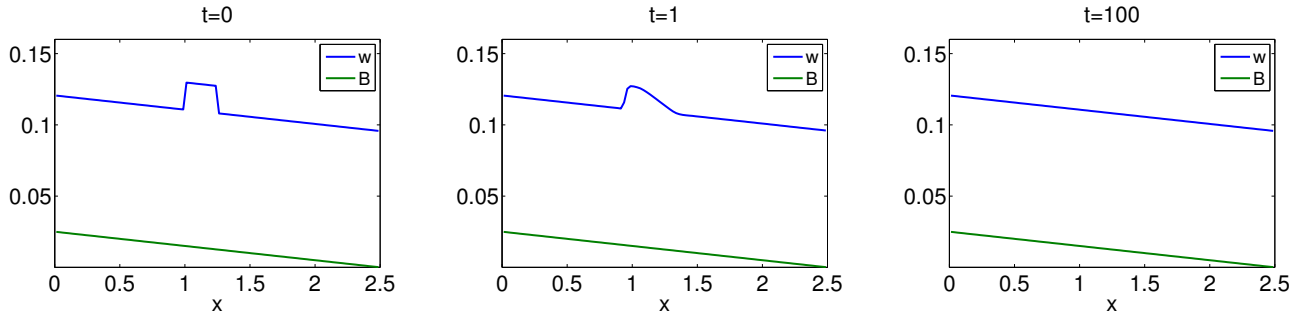

Figure 5.1: Example 2: Evolution of the solution in the supercritical case.

propagates to the right, eventually leaving the domain. At large times, the computed solution converges to the steady state, see Figure 5.1 (right).

We then proceed with a subcritical case (Test 4 in Table 5.1) and again replace the initial data in Example 1 with (5.1). The evolution of the perturbed solution is shown in Figure 5.2. In this case, the shape of the propagating perturbation is different than in the supercritical case, but at large times the computed solution still converges to the steady state.

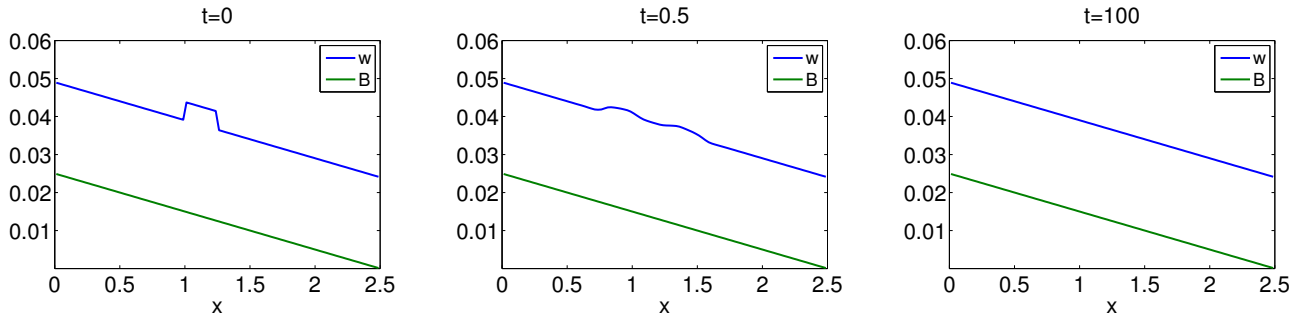

Figure 5.2: Example 2: Evolution of the solution in the subcritical case.

Example 3 – Rainfall-Runoff Over a Slanted Surface. In this example, which is a 1-D modification of Example T3 from [6], we consider a slanted surface, which is originally almost dry:

$$h(x,0)\equiv 10^{-8},\quad (hu)(x,0)\equiv 0. \tag{5.2}$$

The rain of a constant intensity starts falling at time $t = 0$ and stops at time $t = 100$. This is modeled by taking

$$R(x,t) = \begin{cases} 10^{-4}, & 0 \le t \le 100, \\ 0, & \text{otherwise.} \end{cases}$$

The water drains through the right boundary, at which we set a supercritical boundary condition implemented using the ghost cell technique as follows:

$$\left(\overline{h}\right)_{N+1} := \left(\frac{\left(\overline{hu}\right)_N^2}{g}\right)^{1/3}, \quad \left(\overline{hu}\right)_{N+1} := \left(\overline{hu}\right)_N,$$

where N is a total number of cells inside the computational domain $[0, 2.5]$ (we take $N = 100$ in this example). On the left side of the domain we use a solid wall boundary conditions. We consider six sets of data for different values of n and B_x (see Table 5.2) and run the simulations until time $t = 150$ (except for Test 4 in which the final time is $t = 250$).

Test	1	2	3	4	5	6
n	0.02	0.05	0.02	0.05	0.02	0.05
B_x	-0.05	-0.05	-0.01	-0.01	-0.2	-0.2

Table 5.2: The slopes and friction conditions.

In Figure 5.3, we plot the first component of the numerical flux at the right edge of the computational domain ($H^{(1)}_{N+1/2}$) as a function of time. Notice that this is an approximation to the outlet discharge, which is a measurable quantity in experimental settings. In all six cases, the results obtained by the designed central-upwind scheme are in a good agreement with the results reported in [7]. We would like to point out that in [7], the simulations were performed in the 2-D domain of the width 0.2, so that all of the discharge values in Figure 5.3 are to be multiplied by the factor of 0.2 in order to be compared with those in [7]. As one can clearly see from Figure 5.3, the reported results are oscillation-free confirming the robustness of the designed central-upwind scheme.

5.2 Two-Dimensional Examples

Example 4 – Rainfall Runoff Over An Urban Area. We consider another rainfall-runoff example, which now occurs over a more complicated 2-D surface containing houses as outlined in Figure 1.1 (right).

The setting corresponds to the laboratory experiment reported in [6]. The surface structure is shown in Figure 5.4. The experiment was built to mimic an urban area within the laboratory simulator of size $2m \times 2.5m$. To model urban buildings, several blocks were placed onto the surface according to different geometries two of which are shown in Figure 5.4. In these two configurations, the houses are aligned in either the x- (Configuration X20) or y-direction (Configuration Y20). Thus the bottom topography function $B(x,y)$ is defined as

$$B(x,y) = \begin{cases} \mathcal{S}(x,y), & \text{outside the house region,} \\ \mathcal{H}(x,y;x_h,y_h), & \text{inside the house region centered at } (x_h,y_h). \end{cases}$$

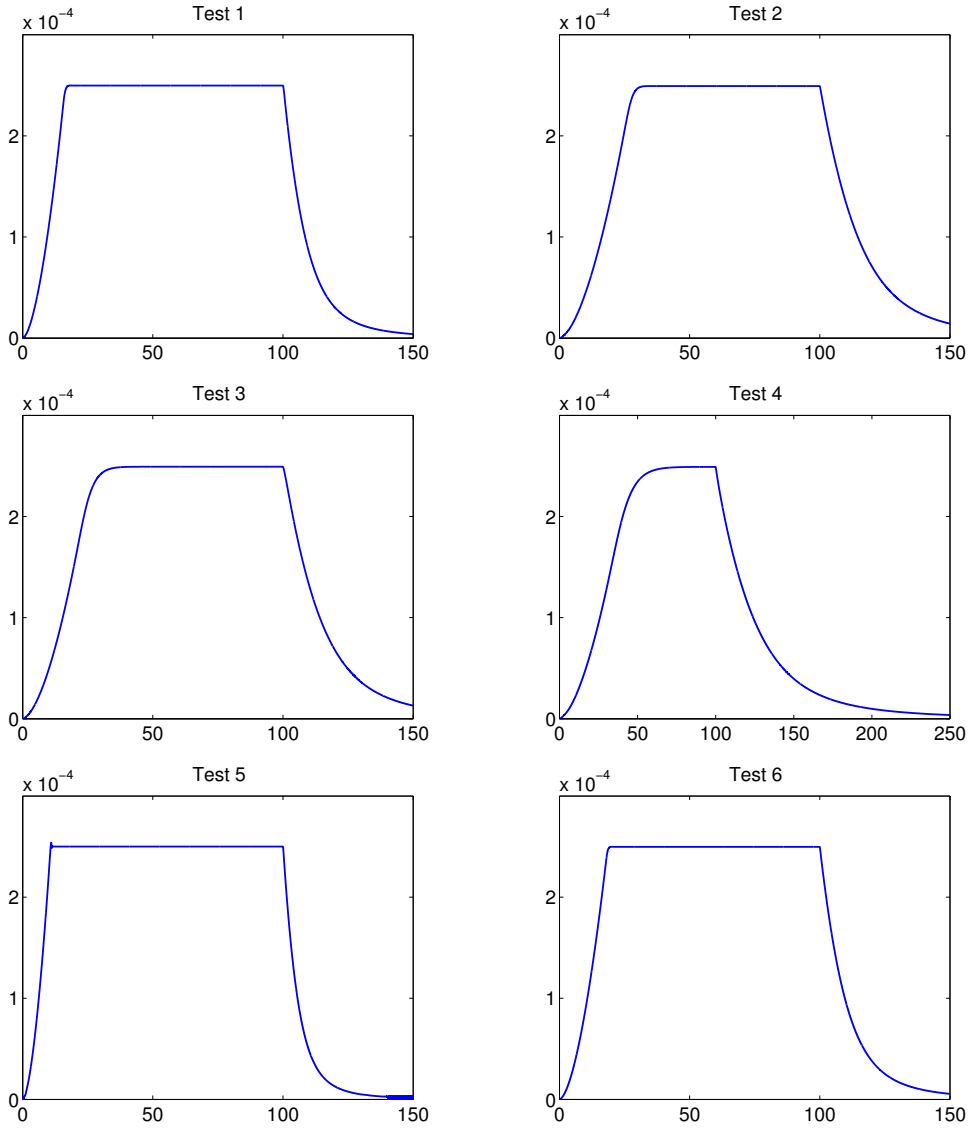

Figure 5.3: Example 3: The outlet discharge as a function of time.

The precise data of surface structure $\mathcal{S}(x, y)$ was provided by Dr. Luis Cea and the house-roof configuration $\mathcal{H}(x, y; x_h, y_h)$ was computed according to the following formulae:

$$\mathcal{H}(x, y; x_h, y_h) = \begin{cases} 0.3 - |y - y_h|, & (x, y) \in [x_h - 0.15, x_h + 0.15] \times [y_h - 0.1, y_h + 0.1], \\ 0, & \text{otherwise}, \end{cases}$$

for Configuration X20 and

$$\mathcal{H}(x, y; x_h, y_h) = \begin{cases} 0.3 - |x - x_h|, & (x, y) \in [x_h - 0.1, x_h + 0.1] \times [y_h - 0.15, y_h + 0.15], \\ 0, & \text{otherwise}, \end{cases}$$

for Configuration Y20. Notice that across the walls of the houses the bottom topography is discontinuous and thus the bilinear interpolant (4.5) has very sharp gradients there.

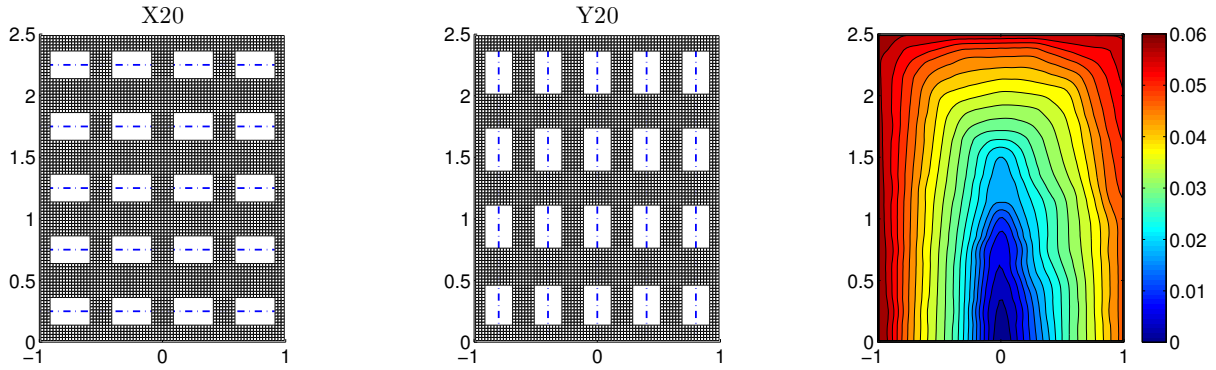

Figure 5.4: Example 4: Two house configurations (X20 and Y20) and contour plot of the urban area topography. In each configuration, the houses are placed in the blank rectangles such that the house ridges coincide with the dash-dotted lines. The figure on the right is the contour plot of the urban area topography.

Similar to the 1-D rainfall-runoff example, we set the almost dry initial conditions:

$$h(x,y,0)\equiv 10^{-8},\quad (hu)(x,y,0)\equiv (hv)(x,y,0)\equiv 0.$$

The rain of a constant intensity starts falling at time $t=0$ and stops at $t=T_s$, that is,

$$R(x,y,t)=\begin{cases}\dfrac{1}{12000}, & 0\le t\le T_s,\\ 0, & \text{otherwise.}\end{cases}$$

In different experiments, different values of $T_s=20$, 40 or 60 have been taken. The computational domain $[-1,1]\times[0,2.5]$ is divided into $N_x\times N_y$ uniform cells (we have taken $N_x=80$ and $N_y=100$). The solid wall boundary conditions have been set at the left, right and top parts of the boundary, while the supercritical boundary conditions have been implemented at the lower part ($-1\le x\le 1$, $y=0$). Namely, we set the following ghost cells values:

$$\bar{h}_{j,0}:=\left(\frac{(\overline{hv})^2_{j,1}}{g}\right)^{1/3},\quad (\overline{hu})_{j,0}:=(\overline{hu})_{j,1},\quad (\overline{hv})_{j,0}:=(\overline{hv})_{j,1},\quad \forall\ 1\le j\le N_x.$$

At this boundary, the total outlet discharge is recorded in the laboratory experiments at different time moments and then it is compared with the computed values of $\sum_{j=1}^{N_x}\left(H^y_{j,1/2}\right)^{(1)}$.

In Figure 5.5, the outlet discharge is plotted as a function of time and compared with the experimental data provided to us by Dr. Luis Cea. Notice that the computed curves there have lower peaks and wider tails then the experimental ones, especially in the case of $T_s=20$.

We believe that such a delay of outlet discharge can be explained by inability of the system (1.2)–(1.4) to accurately model the situation occurring near the house walls where the size of the jumps in the bottom topography is about 2-3 orders of magnitude larger than the water depth. We therefore modify the model by removing the houses from the computational domain and placing the entire rain water, which would accumulate over the houses, near the house walls inside the computational domain. The details of a modified approach are given in Example 4a.

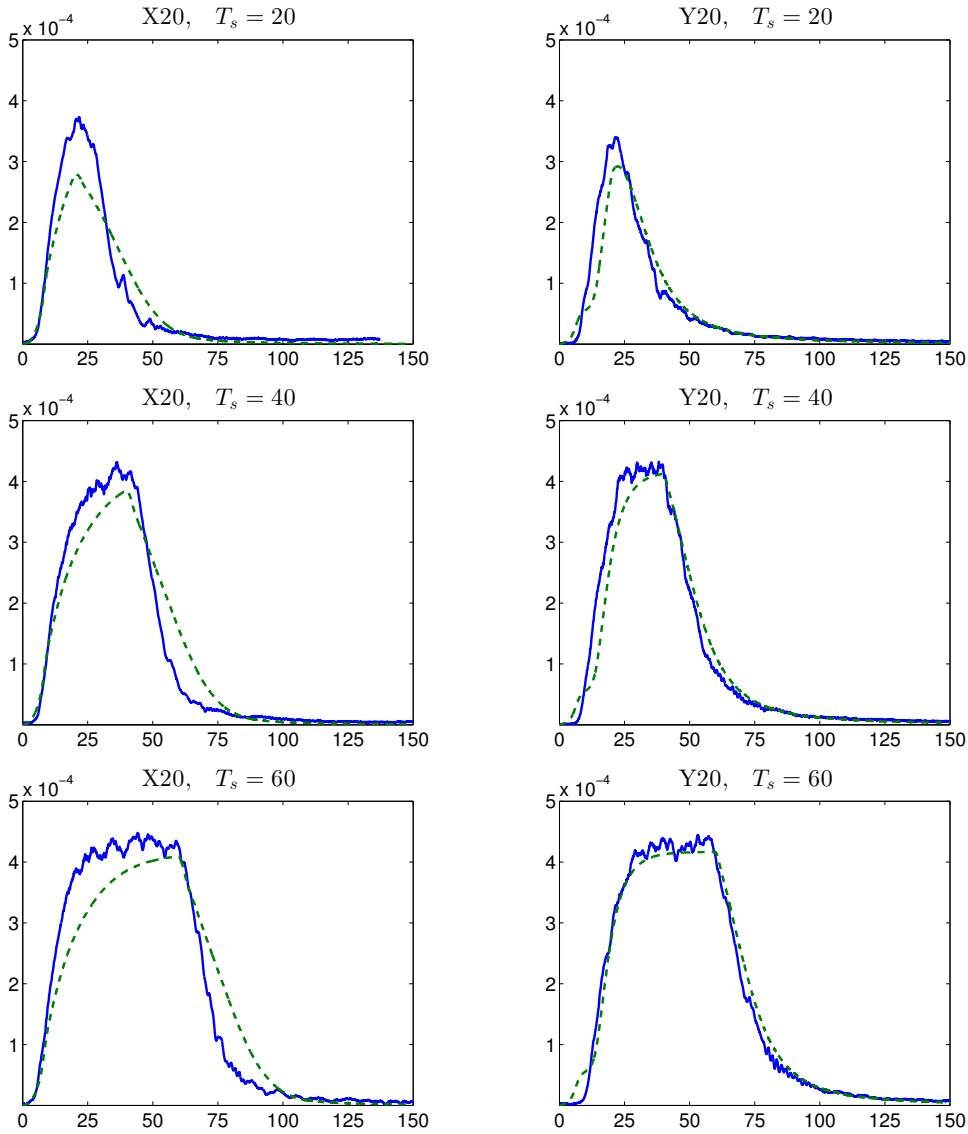

Figure 5.5: Example 4: The outlet discharge (the experimental data, solid line, vs. the computed results, dashed line) as a function of time.

Example 4a – Modified House Treatment. We consider the same setting as in Example 4, but make the following modifications.

First, we remove the houses from the computational domain which becomes a punctured rectangle. Each of the holes is depicted in Figure 5.6: The house walls become the internal boundary, which is numerically treated using a solid wall ghost cell technique. Second, we need to redistribute the rain water falling onto the roof so that it is placed inside the modified computational domain. In the laboratory experiment, the water falling on the house blocks streams down from the long (lower) edges and finally joins the surface water flow, while in reality, the gutter system is commonly used and the rain water streams down from the rain pipes typically located at the house corners.

In the numerical experiments, we adopt two different strategies to mimic the above two draining situations. In both cases, the building-roof rainfall is uniformly distributed on certain cells near

and outside the building edges. These are the shaded cells in Figure 5.6. The modified rain source can then be written as follows:

$$\widehat{R}(x,y,t)=\begin{cases}\dfrac{1}{12000}\left(1+\dfrac{A_h}{A_s}\right), & \text{in the shaded cells,}\\[2ex] \dfrac{1}{12000}, & \text{otherwise,}\end{cases}$$

which is as before switched on only for $t\in[0,T_s]$. Here, A_h is the area of the house, while A_s is the area of the shaded region near that house. If the gutter system is installed, then in both studied configurations (X20 and Y20) with $N_x=80$ and $N_y=100$,

$$\frac{A_h}{A_s}=\frac{0.2\cdot 0.3}{4\Delta x\Delta y}=24.$$

If the gutter system is not installed, then this ratio depends on a house orientation, but since in this numerical example we take $\Delta x=\Delta y=1/40$,

$$\frac{A_h}{A_s}=\frac{0.2}{2\Delta x}=\frac{0.2}{2\Delta y}=4$$

for both Configurations X20 and Y20.

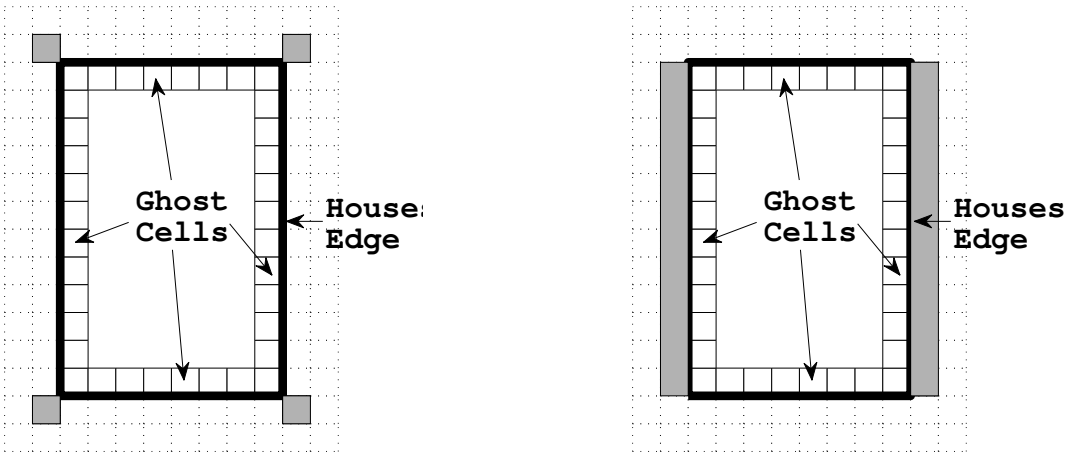

Figure 5.6: Example 4a: A special treatment of a house region. The house edges are implemented as a part of an internal boundary in the shaded cells. The rain-fall on the roof is uniformly distributed in the shaded cells. There are two cases: the one with the gutter system installed (left) and the one without such a system (right).

Again, we compare the outlet discharges obtained by our numerical scheme and the laboratory measurement. As we can see in Figure 5.7, our numerical results are now in much better agreement with the experimental results: The peak height of the outlet discharge is accurately captured in both Configurations X20 and Y20 for $T_s=20$, 40 and 60. It should be also observed that in the case of a longer rain duration ($T_s=60$), the computed outlet discharge remains almost constant

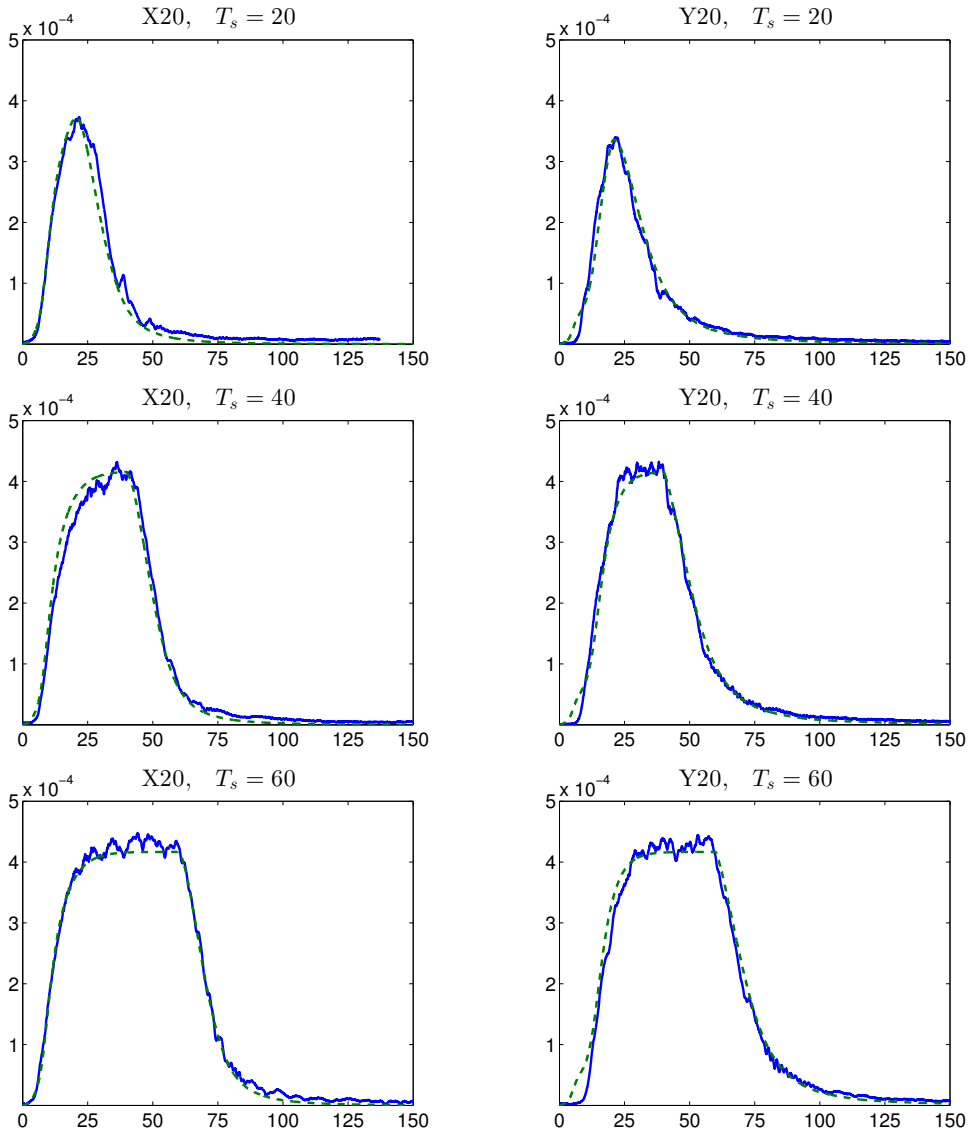

Figure 5.7: Example 4a: The outlet discharge (the experimental data, solid line, vs. the computed results, dashed line) as a function of time.

for $t \in [30, 60]$. In fact, if the rain source is not switched off ($T_s = \infty$), the outlet discharge will converge to a steady state as shown in Figure 5.8. The snapshot of a water height at this steady state is shown in Figure 5.9.

Finally, In Figure 5.10, we plot the water height snapshots at three different times obtained for Configurations X20 and Y20 (we use $T_s = 40$). They show how the rain water drains and it clarifies the dependence of the water flow on the surface configuration. In the examples using Configuration X20, the draining stream takes advantage of the space along the vertical central line $x = 0$ and a big mainstream is formed. In the examples using Configuration Y20, there are houses in the central line $x = 0$ that block the flow there. Therefore, the mainstream of draining water has to bypass these houses and thus small "lakes" are developed behind two of the houses, see Figure 5.10 (lower row).

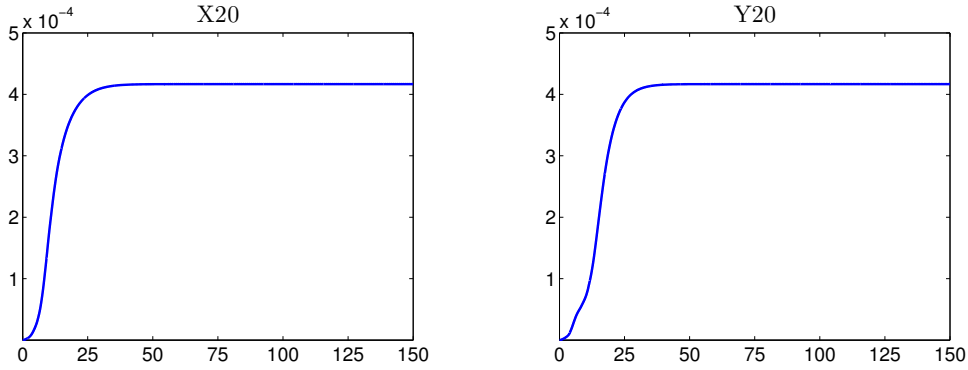

Figure 5.8: Example 4a: The outlet discharge as a function of time: convergence to a steady state when the rain source is not switch off.

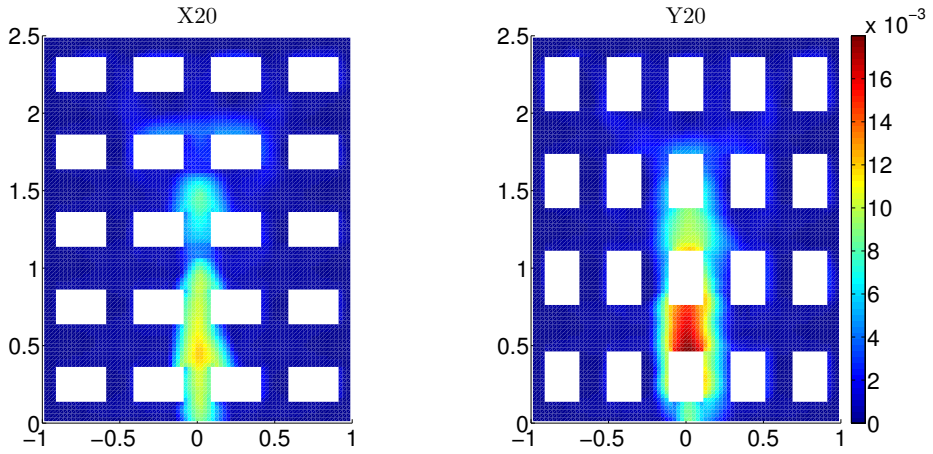

Figure 5.9: Example 4a: The snapshots of water height at the steady state achieved when the rain source is not switched off.

Remark 5.1 We would like to point out that two different strategies of modifying the rain source term near the houses lead to practically the same results. In the reported numerical experiment, we have redistributed the rain falling onto the house into the cells along the longer house edges (see Figure 5.6, right) as discussed in the beginning of Example 4a.

Acknowledgment: The work of A. Chertock was supported in part by the NSF Grant DMS-1216974 and the ONR Grant N00014-12-1-0832. The work of A. Kurganov was supported in part by the NSF Grant DMS-1216957 and the ONR Grant N00014-12-1-0833. The work of S. Cui was supported in part by NSF Grants DMS-1115718 and DMS-1216957. The work of T. Wu was supported in part by the NSF Grant DMS-1115718. A part of this research was conducted during the Summer of 2012, when the authors visited the Institute of Natural Sciences at the Shanghai Jiao Tong University, China. The authors would like to thank the faculty, staff and especially the Institute co-director Prof. Shi Jin for their support and hospitality. The authors also thank Dr. Mario Ricchiuto for encouraging discussions. The authors are thankful to Dr. Luis Cea for providing the experimental data and for his help.

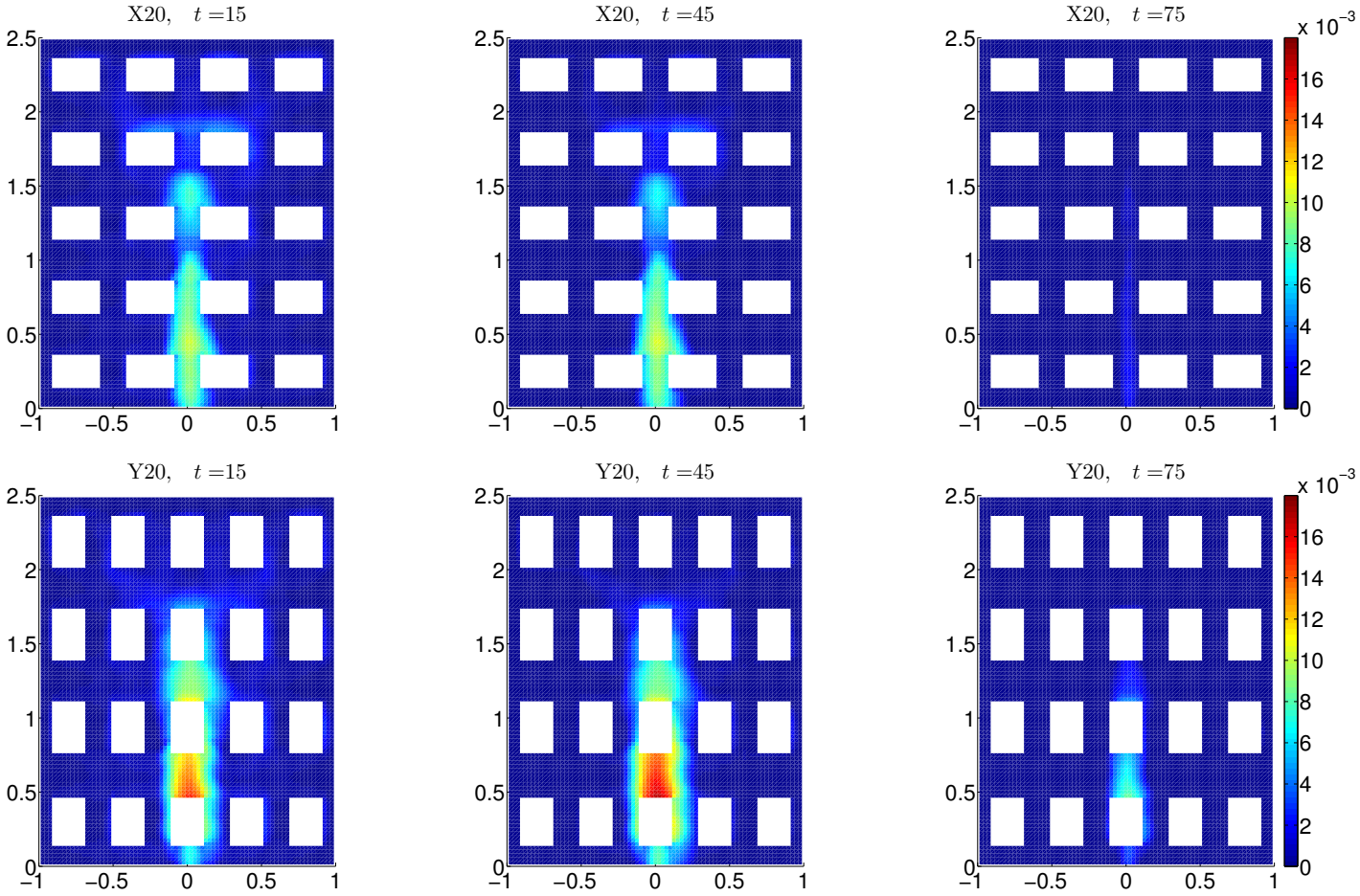

Figure 5.10: Example 4a: Water height snapshots at times $t = 15$, 45 and 75 computed for Configurations X20 and Y20 with $T_s = 40$.

References

[1] E. AUDUSSE, F. BOUCHUT, M.-O. BRISTEAU, R. KLEIN, AND B. PERTHAME, *A fast and stable well-balanced scheme with hydrostatic reconstruction for shallow water flows*, SIAM J. Sci. Comput., 25 (2004), pp. 2050–2065.

[2] C. BERTHON, F. MARCHE, AND R. TURPAULT, *An efficient scheme on wet/dry transitions for shallow water equations with friction*, Comput. & Fluids, 48 (2011), pp. 192–201.

[3] A. BOLLERMANN, G. CHEN, A. KURGANOV, AND S. NOELLE, *A well-balanced reconstruction for wet/dry fronts*, J. Sci. Comput. To appear.

[4] A. BOLLERMANN, S. NOELLE, AND M. LUKÁČOVÁ-MEDVID'OVÁ, *Finite volume evolution Galerkin methods for the shallow water equations with dry beds*, Commun. Comput. Phys., 10 (2011), pp. 371–404.

[5] S. BRYSON, Y. EPSHTEYN, A. KURGANOV, AND G. PETROVA, *Well-balanced positivity preserving central-upwind scheme on triangular grids for the Saint-Venant system*, M2AN Math. Model. Numer. Anal., 45 (2011), pp. 423–446.

[6] L. Cea, M. Garrido, and J. Puertas, *Experimental validation of two-dimensional depth-averaged models for forecasting rainfallrunoff from precipitation data in urban areas*, J. Hydrol., 382 (2010), pp. 88–102.

[7] L. Cea and M. E. Vázquez-Cendón, *Unstructured finite volume discretisation of bed friction and convective flux in solute transport models linked to the shallow water equations*, J. Comput. Phys., 231 (2012), pp. 3317–3339.

[8] A. de Saint-Venant, *Thèorie du mouvement non-permanent des eaux, avec application aux crues des rivière at à l'introduction des marèes dans leur lit.*, C.R. Acad. Sci. Paris, 73 (1871), pp. 147–154.

[9] A. Flamant, *Mécanique appliquée : Hydraulique*, Baudry éditeur, Paris (France), 1891.

[10] J. Gallardo, C. Parés, and M. Castro, *On a well-balanced high-order finite volume scheme for shallow water equations with topography and dry areas*, J. Comput. Phys., 227 (2007), pp. 574–601.

[11] J.-F. Gerbeau and B. Perthame, *Derivation of viscous Saint-Venant system for laminar shallow water; numerical validation*, Discrete Contin. Dyn. Syst. Ser. B, 1 (2001), pp. 89–102.

[12] S. Gottlieb, C.-W. Shu, and E. Tadmor, *Strong stability-preserving high-order time discretization methods*, SIAM Rev., 43 (2001), pp. 89–112.

[13] S. Jin and X. Wen, *Two interface-type numerical methods for computing hyperbolic systems with geometrical source terms having concentrations*, SIAM J. Sci. Comput., 26 (2005), pp. 2079–2101.

[14] R. Kellerhals, *Stable channels with gravel-paved beds*, ASCE Journal of the Waterways and Harbors Division, 93 (1967), p. 6384.

[15] A. Kurganov and D. Levy, *Central-upwind schemes for the saint-venant system*, M2AN Math. Model. Numer. Anal., 36 (2002), pp. 397–425.

[16] A. Kurganov and C.-T. Lin, *On the reduction of numerical dissipation in central-upwind schemes*, Commun. Comput. Phys., 2 (2007), pp. 141–163.

[17] A. Kurganov, S. Noelle, and G. Petrova, *Semi-discrete central-upwind scheme for hyperbolic conservation laws and Hamilton-Jacobi equations*, SIAM J. Sci. Comput., 23 (2001), pp. 707–740.

[18] A. Kurganov and G. Petrova, *A second-order well-balanced positivity preserving central-upwind scheme for the saint-venant system*, Commun. Math. Sci., 5 (2007), pp. 133–160.

[19] ——, *Central-upwind schemes for two-layer shallow equations*, SIAM J. Sci. Comput., 31 (2009), pp. 1742–1773.

[20] A. Kurganov and E. Tadmor, *New high resolution central schemes for nonlinear conservation laws and convection-diffusion equations*, J. Comput. Phys., 160 (2000), pp. 241–282.

[21] ——, *Solution of two-dimensional riemann problems for gas dynamics without riemann problem solvers*, Numer. Methods Partial Differential Equations, 18 (2002), pp. 584–608.

[22] R. LeVeque, *Balancing source terms and flux gradients in high-resolution Godunov methods: the quasi-steady wave-propagation algorithm*, J. Comput. Phys., 146 (1998), pp. 346–365.

[23] R. J. LeVeque, *Finite volume methods for hyperbolic problems*, Cambridge Texts in Applied Mathematics, Cambridge University Press, Cambridge, 2002.

[24] K.-A. Lie and S. Noelle, *On the artificial compression method for second-order nonoscillatory central difference schemes for systems of conservation laws*, SIAM J. Sci. Comput., 24 (2003), pp. 1157–1174.

[25] H. Nessyahu and E. Tadmor, *Nonoscillatory central differencing for hyperbolic conservation laws*, J. Comput. Phys., 87 (1990), pp. 408–463.

[26] S. Noelle, Y. Xing, and C.-W. Shu, *High-order well-balanced schemes*, in Numerical methods for balance laws, vol. 24 of Quad. Mat., Dept. Math., Seconda Univ. Napoli, Caserta, 2009, pp. 1–66.

[27] B. Perthame and C. Simeoni, *A kinetic scheme for the Saint-Venant system with a source term*, Calcolo, 38 (2001), pp. 201–231.

[28] M. Ricchiuto and A. Bollermann, *Stabilized residual distribution for shallow water simulations*, J. Comput. Phys., 228 (2009), pp. 1071–1115.

[29] G. Russo and A. Khe, *High order well balanced schemes for systems of balance laws*, in Hyperbolic problems: theory, numerics and applications, vol. 67 of Proc. Sympos. Appl. Math., Amer. Math. Soc., Providence, RI, 2009, pp. 919–928.

[30] ——, *High order well-balanced schemes based on numerical reconstruction of the equilibrium variables*, in Proceedings "WASCOM 2009" 15th Conference on Waves and Stability in Continuous Media, World Sci. Publ., Hackensack, NJ, 2010, pp. 230–241.

[31] P. Sweby, *High resolution schemes using flux limiters for hyperbolic conservation laws*, SIAM J. Numer. Anal., 21 (1984), pp. 995–1011.

[32] B. van Leer, *Towards the ultimate conservative difference scheme. V. A second-order sequel to Godunov's method*, J. Comput. Phys., 32 (1979), pp. 101–136.

[33] Y. Xing, C.-W. Shu, and S. Noelle, *On the advantage of well-balanced schemes for moving-water equilibria of the shallow water equations*, J. Sci. Comput., 48 (2011), pp. 339–349.